







Quasi-one-dimensional magnetism in the spin- $\frac{1}{2}$ antiferromagnet $\text{BaNa}_2\text{Cu}(\text{VO}_4)_2$

Sebin J. Sebastian ¹, K. Somesh,¹ M. Nandi,² N. Ahmed,¹ P. Bag,¹ M. Baenitz,³ B. Koo ³, J. Sichelschmidt ³,
A. A. Tsirlin ^{4,*}, Y. Furukawa ², and R. Nath ^{1,†}

¹*School of Physics, Indian Institute of Science Education and Research Thiruvananthapuram-695551, India*

²*Ames Laboratory and Department of Physics and Astronomy, Iowa State University, Ames, Iowa 50011, USA*

³*Max Planck Institute for Chemical Physics of Solids, Nöthnitzer Strasse 40, 01187 Dresden, Germany*

⁴*Experimental Physics VI, Center for Electronic Correlations and Magnetism, University of Augsburg, 86135 Augsburg, Germany*



(Received 27 November 2020; revised 12 January 2021; accepted 13 January 2021; published 8 February 2021)

We report synthesis and magnetic properties of quasi-one-dimensional spin- $\frac{1}{2}$ Heisenberg antiferromagnetic chain compound $\text{BaNa}_2\text{Cu}(\text{VO}_4)_2$. This orthovanadate has a centrosymmetric crystal structure, $C2/c$, where the magnetic Cu^{2+} ions form spin chains. These chains are arranged in layers, with the chain direction changing by 62° between the two successive layers. Alternatively, the spin lattice can be viewed as anisotropic triangular layers upon taking the interchain interactions into consideration. Despite this potential structural complexity, temperature-dependent magnetic susceptibility, heat capacity, electron spin resonance intensity, and nuclear magnetic resonance (NMR) shift agree well with the uniform spin-1/2 Heisenberg chain model with an intrachain coupling of $J/k_B \simeq 5.6$ K. The saturation field obtained from the magnetic isotherm measurement consistently reproduces the value of J/k_B . Further, the ^{51}V NMR spin-lattice relaxation rate mimics the one-dimensional character in the intermediate temperature range, whereas magnetic long-range order sets in below $T_N \simeq 0.25$ K. The effective interchain coupling is estimated to be $J_\perp/k_B \simeq 0.1$ K. The theoretical estimation of exchange couplings using band-structure calculations reciprocate our experimental findings and unambiguously establish the one-dimensional character of the compound. Finally, the spin lattice of $\text{BaNa}_2\text{Cu}(\text{VO}_4)_2$ is compared with the chemically similar but not isostructural compound $\text{BaAg}_2\text{Cu}(\text{VO}_4)_2$.

DOI: [10.1103/PhysRevB.103.064413](https://doi.org/10.1103/PhysRevB.103.064413)

I. INTRODUCTION

The studies of low-dimensional and frustrated spin systems have contributed substantially in understanding the quantum phase transitions at low temperatures [1,2]. In one-dimensional (1D) antiferromagnetic (AFM) spin-1/2 uniform Heisenberg chains, magnetic long-range-order (LRO) is forbidden at zero temperature as a result of enhanced quantum fluctuations, thereby exhibiting a gapless excitation spectrum and power-law decay of spin-spin correlations [3]. However, nonzero interchain interactions, inherent to real materials, lead to the formation of magnetic LRO at finite temperatures [4,5]. On the other hand, the interchain interactions often create frustrated network between the chains that eventually prevents the system from achieving the conventional LRO but stabilizes different exotic states instead [2,6–8]. Further, competing interactions as realized in a set of compounds, add magnetic frustration in spin chains which along with quantum fluctuations host a multitude of intriguing magnetic ground states [9–11]. The transition-metal oxides offer nearly endless opportunities for realizing 1D spin chains with different types of exchange couplings and may harbor wide varieties of exotic phases of matter.

Recently, synthesis and magnetic properties of a series of compounds $AA'M(\text{VO}_4)_2$ ($A = \text{Ba}$ and Sr , $A' = \text{Na}_2$ and Ag_2 ,

and $M = \text{Mn}$, Ni , Co , Fe , and Cu) were reported. Despite some variations in their crystal structures, the magnetic model of anisotropic triangular lattice has been generally used to understand their magnetism [12–18]. $\text{BaAg}_2\text{Cu}(\text{VO}_4)_2$ stands as an exception in this series, because its crystal structure is triclinic (space group: $P\bar{1}$) [12], and indeed microscopic analysis via density-functional band-structure calculations [19] combined with resonance spectroscopy [20] revealed 1D magnetism with two dissimilar types of spin chains, one ferromagnetic and one antiferromagnetic, coexisting in the structure.

Here, we present the magnetic properties of $\text{BaNa}_2\text{Cu}(\text{VO}_4)_2$, another Cu^{2+} member of the series [21]. Its structure features four equal Cu-Cu distances of 5.507 Å as well as two slightly longer distances of 5.686 Å, all in the ab plane. This interaction geometry is a prerequisite of the triangular-lattice scenario previously established for other members of the $AA'M(\text{VO}_4)_2$ series. On the other hand, the square-planar oxygen coordination of Cu^{2+} and the VO_4 bridges between such CuO_4 plaquette units may lead to one preferred direction for magnetic couplings in the ab plane (Fig. 1). Interestingly, this preferred direction changes from $\mathbf{a} + \mathbf{b}$ in one plane to $\mathbf{a} - \mathbf{b}$ in the adjacent plane, thus leading to the formation of crossed spin chains arranged at 62° relative to each other. This geometry resembles the crossed-chain magnetic model, where exotic ground states and potential spin-liquid behavior have been proposed theoretically [22–26].

*altsirlin@gmail.com

†rnath@iisertvm.ac.in

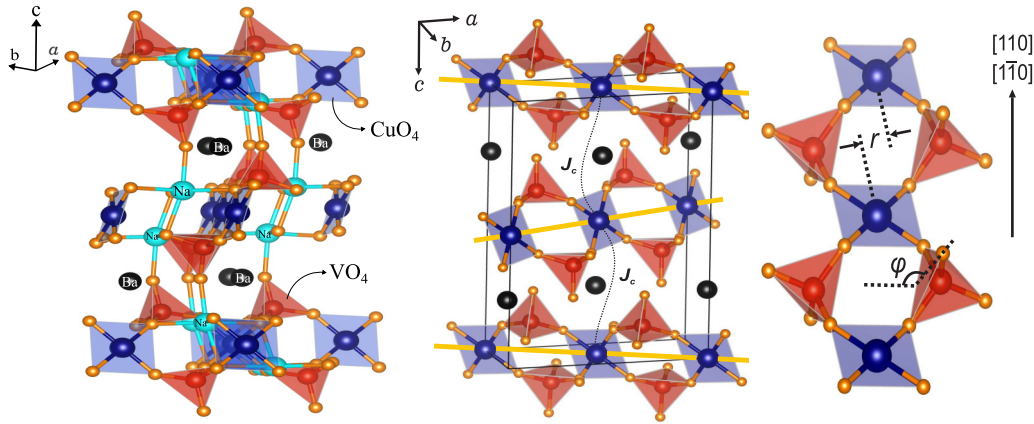


FIG. 1. Left panel: crystal structure of $\text{BaNa}_2\text{Cu}(\text{VO}_4)_2$ showing corner-shared CuO_4 plaquettes and VO_4 tetrahedra forming layers of spin chains. The coupling of Na^{1+} ions with the magnetic Cu^{2+} ions is also shown. Middle panel: crystal structure of $\text{BaNa}_2\text{Cu}(\text{VO}_4)_2$ shown in a different orientation to visualize the spin chains running along the $[110]$ and $[1\bar{1}0]$ directions; black spheres show the Ba atoms, the Na atoms are omitted for clarity. Right panel: the structure of the single spin chain with the geometrical parameters φ and r that control the sign and strength of superexchange through the double bridges of the VO_4 tetrahedra.

Here, we use magnetization, heat capacity, electron spin resonance (ESR), and nuclear magnetic resonance (NMR) measurements, as well as complementary band-structure calculations to uncover magnetic interactions in $\text{BaNa}_2\text{Cu}(\text{VO}_4)_2$ and establish its microscopic magnetic model. Our data suggest the formation of uniform AFM spin chains with the exchange coupling $J/k_B \simeq 5.6$ K and the subsequent onset of magnetic LRO below $T_N \simeq 0.25$ K. We suggest that this magnetic order can be driven by residual interchain couplings of $J_\perp/k_B \simeq 0.1$ K that remain non-frustrated despite the crossed-chain structural geometry. Our results establish that the mere presence of spin chains arranged along two different directions is insufficient to reach the interesting physics of the crossed-chain model, and an additional condition for the lateral displacement of these chains has to be met experimentally.

II. METHODS

Polycrystalline sample of $\text{BaNa}_2\text{Cu}(\text{VO}_4)_2$ was prepared by the usual solid-state reaction method. Initially, the reactants Na_2CO_3 (Aldrich, 99.995%), BaCO_3 (Aldrich, 99.995%), CuO (Aldrich, 99.999%), and V_2O_5 (Aldrich, 99.995%) were mixed in proper molar ratios, thoroughly ground, and then pressed into pellets. The pellets were sintered in an alumina crucible at 500°C for three days in air with several intermediate grindings. The phase purity of the sample was confirmed from the powder x-ray diffraction (XRD) performed at room temperature. For the powder XRD experiment, a PANalytical powder diffractometer with $\text{CuK}\alpha$ radiation ($\lambda_{\text{avg}} \simeq 1.54182$ Å) was used. Le-Bail analysis of the powder XRD pattern was performed using the FULLPROF software package [27]. Figure 2 displays the room-temperature powder XRD data along with the fit. The structural parameters given in Ref. [21] were used as the initial parameters. The goodness-of-fit was found to be $\chi^2 \simeq 3.57$. The obtained lattice parameters are $a = 9.4379(1)$ Å, $b = 5.6926(1)$ Å, $c = 14.0519(1)$ Å, and $\beta = 92.3434(8)^\circ$ and the unit cell volume $V_{\text{cell}} \simeq 754.34$ Å³, which are in close agreement with the previous report [21].

Magnetization (M) measurements were performed as a function of temperature ($0.48 \text{ K} \leq T \leq 380 \text{ K}$) and magnetic field ($0 \leq H \leq 14 \text{ T}$) using a superconducting quantum interference device (SQUID, Quantum Design) magnetometer and a physical property measurement system (PPMS, Quantum Design). The SQUID enabled us to measure magnetization down to 0.48 K with a ^3He attachment. High-field magnetization up to 14 T were measured using PPMS. Heat capacity (C_p) was measured as a function of T ($0.4 \text{ K} \leq T \leq 200 \text{ K}$) on a sintered pellet using the thermal relaxation method in PPMS. The temperature down to 0.4 K was achieved using a ^3He attachment to the PPMS.

The ESR experiments were performed on the powder sample with a standard continuous-wave spectrometer in the temperature range $2.5 \text{ K} \leq T \leq 300 \text{ K}$. As a function of external magnetic field B , the resonance shows up as an absorbed power P of a transversal magnetic microwave field ($\nu \simeq 9.4 \text{ GHz}$, X band). In order to improve the signal-to-

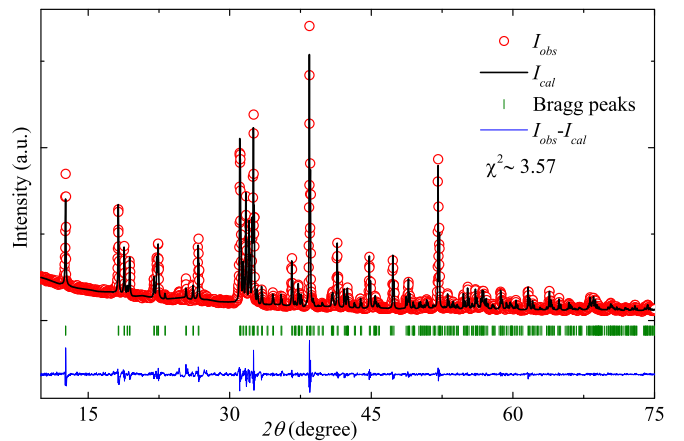


FIG. 2. Powder XRD pattern of $\text{BaNa}_2\text{Cu}(\text{VO}_4)_2$ measured at $T = 300 \text{ K}$. The circles are experimental data and the solid black line is the Le-Bail fit. The Bragg positions are indicated by green vertical lines and the bottom solid blue line indicates the difference between the experimental and calculated intensities.

noise ratio, a lock-in technique was used by modulating the applied field, which yields the derivative of power absorption dP/dB as a function of B . By using the resonance condition $g = \frac{h\nu}{\mu_B H_{\text{res}}}$, where h is the Planck's constant, μ_B is the Bohr magneton, ν is the resonance frequency, and H_{res} is the corresponding resonance field, the g value was obtained.

The pulsed NMR measurements were performed on both ^{23}Na (nuclear spin $I = 3/2$ and gyromagnetic ratio $\gamma = 11.26$ MHz/T) and ^{51}V ($I = 7/2$ and $\gamma = 11.19$ MHz/T) nuclei in the temperature range $0.044 \text{ K} \leq T \leq 200 \text{ K}$. For measurements above 2 K a ^4He cryostat (Oxford Instrument) with a field-sweep superconducting magnet was used, while for measurements in the low-temperature range ($0.044 \text{ K} \leq T \leq 2 \text{ K}$), a $^3\text{He}/^4\text{He}$ dilution refrigerator (Kelvinox, Oxford Instruments) with a field sweep magnet was used. All the NMR measurements were carried out in a radio frequency of 77 MHz. The NMR spectra were measured as a function of temperature T by sweeping the magnetic field at a constant radio frequency of 77 MHz. The NMR shift was calculated for both ^{23}Na and ^{51}V nuclei as $K(T) = [H_{\text{ref}} - H(T)]/H(T)$, where H is the resonance field for ^{23}Na and ^{51}V and H_{ref} is the resonance field of the nonmagnetic reference sample. The spin-lattice relaxation rate $1/T_1$ was measured by the conventional single saturation pulse method.

Density-functional (DFT) band-structure calculations were performed in the FPL0 code [28] using the structural parameters from Ref. [21] and local-density approximation (LDA) for the exchange-correlation potential [29]. Exchange parameters of the spin Hamiltonian

$$\mathcal{H} = \sum_{\langle ij \rangle} J_{ij} \mathbf{S}_i \mathbf{S}_j \quad (1)$$

with $S = \frac{1}{2}$ and the summation over atomic pairs $\langle ij \rangle$, were extracted via two complementary procedures. First, band structure obtained on the LDA level was mapped onto a tight-binding model for the half-filled $d_{x^2-y^2}$ orbitals of Cu^{2+} as the magnetic ion. Squared hopping parameters t_i of this tight-binding model are proportional to AFM contributions to the exchange, $J_i^{\text{AFM}} = 4t_i^2/U_{\text{eff}}$, where U_{eff} is the effective onsite Coulomb repulsion. Alternatively, full exchange couplings J_i comprising both FM and AFM contributions are extracted by a mapping procedure [30] from total energies of magnetically ordered states calculated on the DFT + U level, with correlation effects in the Cu 3d shell modeled by the onsite Coulomb repulsion $U_d = 6 \text{ eV}$, Hund's exchange $J_d = 1 \text{ eV}$, and around-mean-field flavor of the double-counting correction [19,31]. The k mesh with up to 150 points in the symmetry-irreducible part of the first Brillouin zone was used.

Field-dependent magnetization and magnetic specific heat of a uniform spin- $\frac{1}{2}$ chain were obtained from quantum Monte-Carlo simulations for $L = 32$ finite lattices with periodic boundary conditions. The loop [32] and dirloop_sse [33] algorithms of the ALPS simulation package [34] were used.

III. RESULTS AND DISCUSSION

A. Magnetization

Temperature-dependent magnetic susceptibility $\chi(T)$ ($= M/H$) of the polycrystalline $\text{BaNa}_2\text{Cu}(\text{VO}_4)_2$ sample mea-

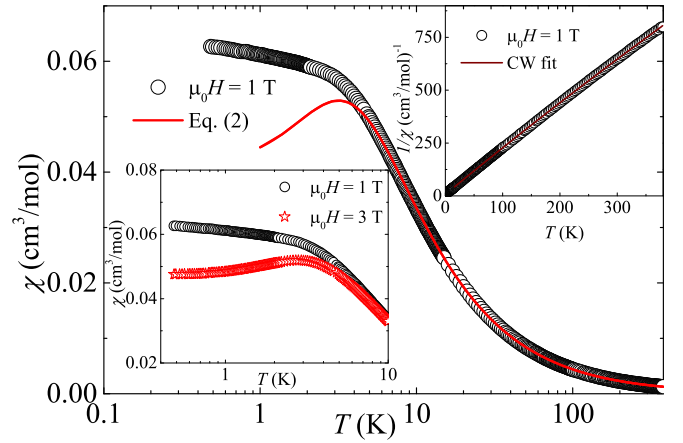


FIG. 3. χ of polycrystalline $\text{BaNa}_2\text{Cu}(\text{VO}_4)_2$ sample as a function of temperature in an applied field $\mu_0 H = 1 \text{ T}$. The solid line is the fit using Bonner-Fisher model [Eq. (2)] for uniform Heisenberg spin- $1/2$ chain. Upper inset: inverse susceptibility $1/\chi$ vs T and the solid line represents the CW fit, as discussed in the text. Lower inset: the low-temperature $\chi(T)$ measured in two different fields $\mu_0 H = 1 \text{ T}$ and 3 T .

sured in two different applied fields $H = 1 \text{ T}$ and 3 T is depicted in Fig. 3. The most significant feature in the $\chi(T)$ curve is the presence of a broad maximum at 3 K, signaling a crossover to an AFM short-range ordered state, typical for low-dimensional spin systems [35,36]. This broad maximum is more pronounced in the 3 T data shown in the lower inset of Fig. 3. No anomaly indicative of the potential LRO could be seen down to 0.48 K.

The preliminary analysis was done by fitting the $\chi(T)$ data using the Curie-Weiss (CW) law, $\chi(T) = \chi_0 + C/(T + \theta_{\text{CW}})$, where χ_0 is the temperature-independent susceptibility, C is the Curie constant, and θ_{CW} is the characteristic CW temperature. The fit shown in the upper inset of Fig. 3 in the high-temperature regime ($T \geq 16 \text{ K}$) yields the following parameters: $\chi_0 \simeq 7.9288 \times 10^{-5} \text{ cm}^3/\text{mol}$, $C \simeq 0.445 \text{ cm}^3\text{K}/\text{mol}$, and $\theta_{\text{CW}} \simeq 3 \text{ K}$. In order to estimate the Van-Vleck paramagnetic susceptibility (χ_{VV}), which arises from the second-order contribution to free energy in the presence of magnetic field, core diamagnetic susceptibility χ_{core} of $\text{BaNa}_2\text{Cu}(\text{VO}_4)_2$ was calculated to be $-1.57 \times 10^{-4} \text{ cm}^3/\text{mol}$ by summing the core diamagnetic susceptibilities of individual ions Na^+ , Ba^{2+} , Cu^{2+} , V^{5+} , and O^{2-} [37,38]. Subsequently, χ_{VV} was obtained by subtracting χ_{core} from χ_0 to be $\sim 2.36 \times 10^{-4} \text{ cm}^3/\text{mol}$, which is close to the values reported for other cuprates [39–41] and consistent with tetragonal crystal-field splitting at the Cu^{2+} site with the square-planar oxygen coordination [42].

From the Curie constant C , the effective moment is calculated using the relation $\mu_{\text{eff}} = \sqrt{3k_B C/N_A}$ to be $\simeq 1.88 \mu_B$, where k_B is the Boltzmann constant, μ_B is the Bohr magneton, and N_A is the Avogadro's number. For a spin- $\frac{1}{2}$ system, the spin-only effective moment is expected to be $\mu_{\text{eff}} = g\sqrt{S(S+1)}\mu_B \simeq 1.73 \mu_B$, assuming Landé g factor $g = 2$. However, our experimental value of $\mu_{\text{eff}} \simeq 1.88 \mu_B$ corresponds to a g factor of $g \simeq 2.17$, which is consistent with the ESR experiments discussed later. The positive value of θ_{CW}

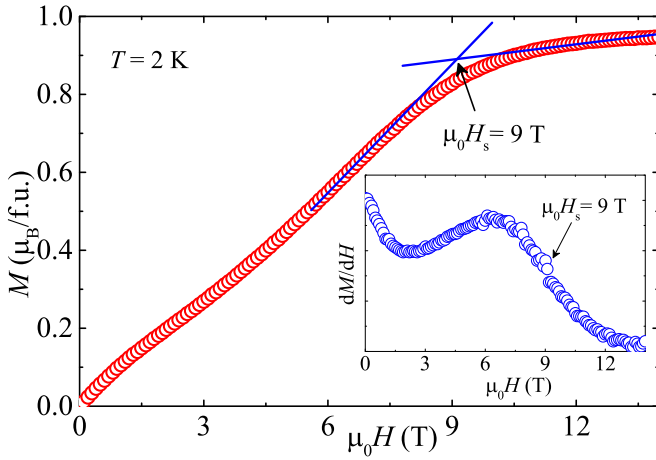


FIG. 4. Magnetization (M) vs H measured at $T = 2$ K. Inset: dM/dH vs H to highlight the saturation field H_s .

suggests that the dominant exchange interactions between the Cu^{2+} ions are AFM in nature.

In order to estimate the exchange coupling between the Cu^{2+} ions, we decomposed $\chi(T)$ into three components,

$$\chi(T) = \chi_0 + \frac{C_{\text{imp}}}{T} + \chi_{\text{spin}}(T). \quad (2)$$

Here, the second term is the Curie law, which accounts for the paramagnetic contributions from impurity spins and/or defects, and $\chi_{\text{spin}}(T)$ is the intrinsic spin susceptibility. This last term can be chosen in different forms depending on the underlying magnetic model. The best fit was achieved with the spin-chain model, which is further supported by the specific-heat data (Sec. III C) and *ab initio* calculations (Sec. III E).

The susceptibility of a spin- $\frac{1}{2}$ uniform Heisenberg AFM chain takes the form

$$\chi_{\text{spin}} = \frac{N_A \mu_B^2 g^2}{k_B T} \frac{0.25 + 0.0775x + 0.0752x^2}{1 + 0.993x + 0.1721x^2 + 0.7578x^3}, \quad (3)$$

with $x = |J|/k_B T$ [35]. This is simply a high-temperature series expansion (HTSE) valid in the regime $k_B T/J \geq 0.5$. The solid line in Fig. 3 represents the best fit of the $\chi(T)$ data above 4 K by Eq. (2). The following parameters were obtained: $\chi_0 \simeq 1.44 \times 10^{-4}$ cm³/mol, $C_{\text{imp}} \simeq 0.0258$ cm³K/mol, $g \simeq 2.13$, and the dominant intrachain AFM exchange coupling $J/k_B \simeq 5.6$ K. From the value of C_{imp} , the sample was found to contain $\sim 6\%$ spin- $\frac{1}{2}$ impurities/defects. At temperatures below 1 K, this impurity contribution becomes dominant and causes the reduction in the susceptibility with the applied field, even though $\chi_{\text{spin}}(T)$ should increase when the field is applied [43].

The magnetic isotherm at $T = 2$ K up to 14 T is shown in Fig. 4. M increases almost linearly with H but with a small curvature. It develops a tendency of saturation above 9 T. A more accurate value of the saturation field $H_s \simeq 9$ T was found by drawing tangential at the curvature (see Fig. 4). The field derivative of the M vs H plot also implies $H_s \simeq 9$ T (see the inset of Fig. 4). For a spin-1/2 Heisenberg AFM chain, the saturation field is directly proportional to the intrachain exchange coupling as $H_s = 2J_{1D}/(k_B/g\mu_B)$ [44]. Using the value of $J/k_B \simeq 5.6$ K, the saturation field is calculated to be

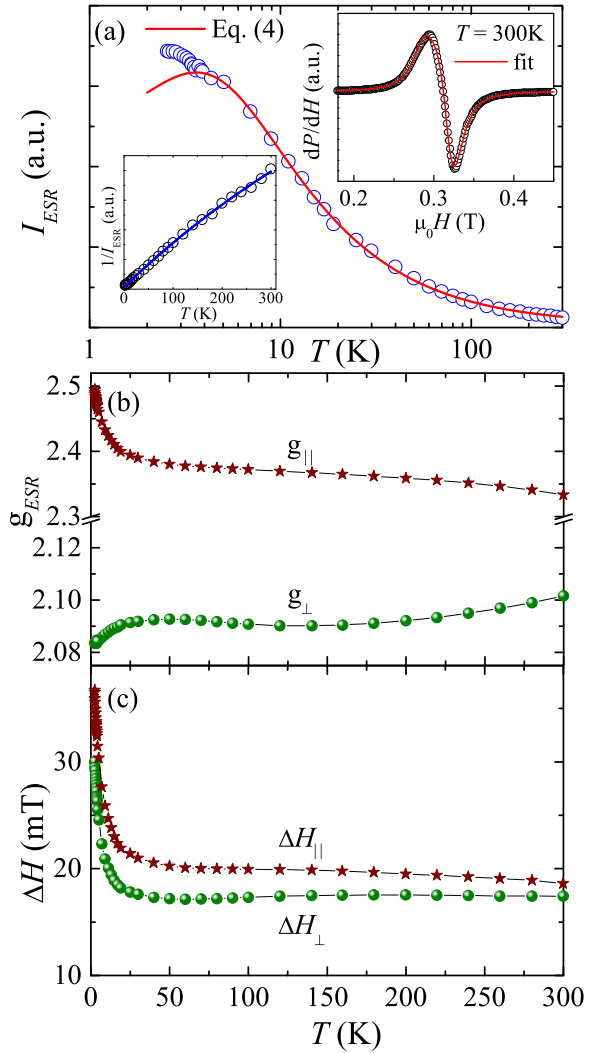


FIG. 5. (a) Integrated ESR intensity vs temperature and the solid line represents the fit as described in the text. Inset: ESR spectrum at room temperature measured at a microwave frequency of 9.4 GHz together with the powder-averaged Lorentzian fit (solid line). (b) Temperature variation of the g values (both perpendicular and parallel components) obtained from the Lorentzian fit. (c) Temperature-dependent ESR linewidth ΔH (both perpendicular and parallel components).

$H_s \simeq 8.34$ T, which matches well with the experimental value, confirming the dominant 1D character of the compound.

B. ESR

ESR experiment was performed on the powder sample and the results are shown in Fig. 5. The inset of Fig. 5(a) depicts a typical ESR powder spectrum at 300 K. The uniaxial g factor anisotropy was obtained by fitting the spectra using the powder-averaged Lorentzian line. The fit of the spectrum at room temperature yields the anisotropic g -tensor components $g_{||} = 2.33(3)$ and $g_{\perp} = 2.10(2)$. From these values, the average g value was calculated as $g = [(g_{||} + 2g_{\perp})/3] = 2.17(3)$ [45]. This value is slightly larger ($\Delta g/g \simeq 0.085$) compared to the free electron value ($g = 2$), typical for Cu^{2+} based oxides [46,47]. The integrated ESR intensity (I_{ESR}) obtained

from the above fit is plotted as a function of temperature in Fig. 5(a). It shows similitude with the $\chi(T)$ behavior, which traces a broad maximum at around $T_{\text{ESR}}^{\text{max}} \simeq 3.7$ K. Indeed, the I_{ESR} vs χ plot with temperature as an implicit parameter follows a straight line down to ~ 5 K (not shown). The variation of g with respect to temperature is shown in Fig. 5(b). Both the components of g were found to be almost temperature independent at high temperatures ($T \geq 20$ K). However, below 20 K a weak deviation from the room-temperature values is observed.

In order to estimate the exchange coupling, $I_{\text{ESR}}(T)$ was fitted by

$$I_{\text{ESR}}(T) = A + B\chi_{\text{spin}}(T). \quad (4)$$

Here, A and B are arbitrary constants, and χ_{spin} is given by Eq. (3). Our fit (see Fig. 5) in the high-temperature regime ($T \geq 5$ K) produced $J/k_B \simeq 5.55$ K. This value of J/k_B is close to the one obtained from the $\chi(T)$ analysis. During the fit, the value of g was kept constant to 2.17, as obtained above. We have also fitted the $1/I_{\text{ESR}}$ data in the high-temperature regime ($T \geq 10$ K) using the relation $I_{\text{ESR}} = M + N/(T + \theta_{\text{CW}})$ where M and N are arbitrary constants. As shown in the lower inset of Fig. 5(a), the fit returns $\theta_{\text{CW}} \simeq 3.9$ K, which is in good agreement with the value obtained from the $\chi^{-1}(T)$ analysis.

The temperature-dependent ESR linewidth, or equivalently the half width at half maximum of the ESR absorption signal, is presented in Fig. 5(c). Both the parallel (ΔH_{\parallel}) and perpendicular (ΔH_{\perp}) components of the ESR line width follow the general trend, commonly observed in most of the low-dimensional spin systems [48,49]. The rapid increase/divergence below ~ 25 K indicates the growth of strong spin correlations at low temperatures as the system approaches the magnetic LRO state.

C. Heat capacity

Temperature-dependent heat capacity C_p of the polycrystalline sample is shown in the upper panel of Fig. 6. In magnetic insulators, the two major contributions to C_p are from phonon and magnetic parts. At high temperatures, $C_p(T)$ is dominated by the phonon part, while at low temperatures it is dominated by the magnetic part. Our experimental C_p data exhibit a pronounced broad maximum at $T \simeq 2.5$ K indicative of the low-dimensional short-range order and also reflects the dominant magnetic contribution at low temperatures. In order to estimate the magnetic contribution to the heat capacity C_{mag} , we proceed as follows. First we approximate the lattice contribution C_{ph} by fitting the high-temperature data by a linear combination of one Debye and two Einstein terms (Debye-Einstein model) as [50,51]

$$C_{\text{ph}}(T) = f_D C_D(\theta_D, T) + \sum_{i=1}^2 g_i C_{E_i}(\theta_{E_i}, T). \quad (5)$$

The first term in Eq. (5) is the Debye term,

$$C_D(\theta_D, T) = 9nR \left(\frac{T}{\theta_D} \right)^3 \int_0^{\frac{\theta_D}{T}} \frac{x^4 e^x}{(e^x - 1)^2} dx. \quad (6)$$

Here, $x = \frac{\hbar\omega}{k_B T}$, ω is the vibration frequency, R is the universal gas constant, and θ_D is the characteristic Debye temperature.

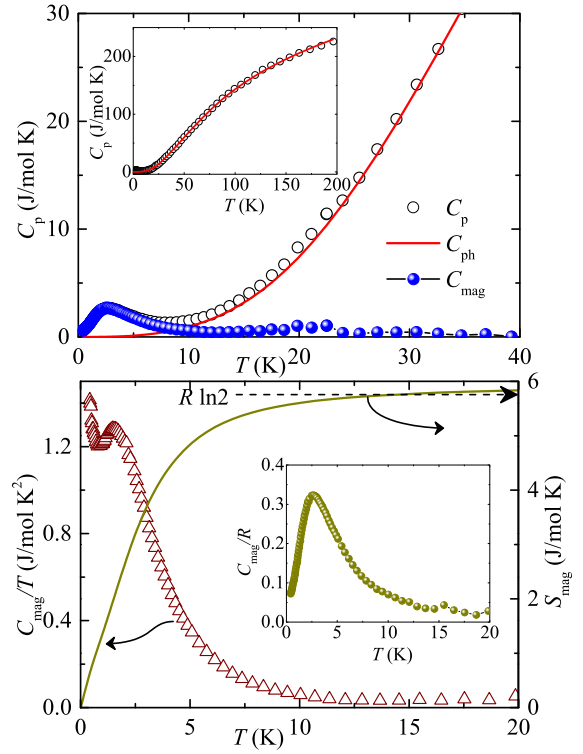


FIG. 6. Upper panel: Heat capacity (C_p) vs T in zero applied field. The solid line denotes the phonon contribution to the heat capacity C_{ph} using the Debye-Einstein fit. The blue solid spheres indicate the magnetic contribution to the heat capacity C_{mag} . Inset: C_p vs T in the whole measured temperature range along with the Debye-Einstein fit. Lower panel: The left y axis shows C_{mag}/T and the right y axis shows the magnetic entropy S_{mag} vs T . Inset: C_{mag}/R vs T .

The second term in Eq. (5) is a combination of the Einstein terms that are usually responsible for flat optical modes in the phonon spectrum,

$$C_E(\theta_E, T) = 3nR \left(\frac{\theta_E}{T} \right)^2 \frac{e^{\theta_E/T}}{(e^{\theta_E/T} - 1)^2}. \quad (7)$$

Here, θ_E is the characteristic Einstein temperature. The coefficients f_D , g_1 , and g_2 are the weight factors, which take into account the number of atoms per formula unit (n) and are conditioned such that at high temperatures the Dulong-Petit value of $3nR$ is satisfied. The $C_p(T)$ data above ~ 15 K were fitted by Eq. (5) and the obtained parameters are $f_D \simeq 0.34$, $g_1 \simeq 0.35$, and $g_2 \simeq 0.31$, $\theta_D \simeq 214$ K, $\theta_{E_1} \simeq 356$ K, and $\theta_{E_2} \simeq 897$ K. Further Einstein terms beyond θ_{E_2} rendered the fit unstable. The fit itself is phenomenological in nature, although one may tentatively associate θ_D with low-energy vibrations of heavier atoms (Ba, Cu, and V) that constitute 28.5%, about $\frac{1}{3}$ of the atomic species in $\text{BaNa}_2\text{Cu}(\text{VO}_4)_2$. The lower Einstein temperature θ_{E_1} may correspond to Na atoms and two apical oxygens of the VO_4 tetrahedra (altogether six atoms per formula unit), whereas θ_{E_2} reflects higher-energy vibrations of the remaining four oxygens that are bound to V and Cu at the same time.

The high- T fit was extrapolated down to low temperatures and $C_{\text{mag}}(T)$ was estimated by subtracting $C_{\text{ph}}(T)$ from $C_p(T)$

[see Fig. 6 (upper panel)]. $C_{\text{mag}}(T)/T$ was plotted as a function of temperature in the lower panel of Fig. 6. The broad maximum corresponding to the short-range order is apparent at $T \simeq 1.52$ K. At low temperatures, $C_{\text{mag}}(T)/T$ shows a rapid increase, which could be related to the onset of magnetic LRO below 0.4 K. The magnetic entropy was calculated as $S_{\text{mag}}(T) = \int_2^T \frac{C_{\text{mag}}(T')}{T'} dT'$, which yields $S_{\text{mag}} \simeq 5.83$ J/mol K at 20 K (see the lower panel of Fig. 6). This value is close to the expected magnetic entropy for spin- $\frac{1}{2}$: $S_{\text{mag}} = R \ln 2 = 5.76$ J/mol K.

In the inset of the lower panel of Fig. 6, C_{mag}/R is plotted against T . The peak of C_{mag}/R can be used to discriminate between different microscopic scenarios. Its height depends on the nature of the underlying spin lattice [52]. Our experimental peak value of $C_{\text{mag}}/R \simeq 0.323$ fits well to the aforementioned 1D scenario, suggesting that VO_4 bridges choose the direction of spin chains. Alternatively, four shortest Cu-Cu contacts of 5.507 Å could cause interactions of equal strength and form a 2D square-lattice interaction topology that should manifest itself by a much higher peak with $C_{\text{mag}}/R \simeq 0.47$. On the other hand, the triangular-lattice scenario would reduce the peak value to $C_{\text{mag}}/R \simeq 0.22$, lower than seen experimentally. We thus conclude that our specific-heat data favor the spin-chain scenario for $\text{BaNa}_2\text{Cu}(\text{VO}_4)_2$.

D. ^{23}Na and ^{51}V NMR

NMR is a potent tool to study the static and dynamic properties of spin systems. In $\text{BaNa}_2\text{Cu}(\text{VO}_4)_2$, the ^{23}Na and ^{51}V nuclei are hyperfine coupled to the magnetic Cu^{2+} ions along the spin chains. Therefore, the low-lying excitations of Cu^{2+} spins can be probed by means of ^{23}Na and ^{51}V NMR measurements. The quadrupole nuclei ^{23}Na ($I = 3/2$) and ^{51}V ($I = 7/2$) are in a noncubic symmetry that may produce an asymmetric charge distribution and hence electric field gradient (EFG). Therefore, the fourfold and eightfold degeneracies of the $I = 3/2$ and $I = 7/2$ spins, respectively, are lifted partially due to the interaction between the nuclear quadrupole moment (Q) and the surrounding EFG. In this case, the nuclear spin Hamiltonian is a sum of the Zeeman and quadrupolar interaction terms [53,54],

$$\mathcal{H} = -\gamma \hbar \hat{I} H (1 + K) + \frac{h\nu_Q}{6} [(3\hat{I}_z^2 - \hat{I}^2) + \eta(\hat{I}_x^2 - \hat{I}_y^2)]. \quad (8)$$

Here, the nuclear quadrupole resonance (NQR) frequency is defined as $\nu_Q = \frac{3e^2qQ}{2I(2I-1)\hbar}$, e is the electron charge, $\hbar (= h/2\pi)$ is the Planck's constant, H is the applied field along \hat{z} , K is the magnetic shift due to hyperfine field at the nuclear site, $V_{\alpha\beta}$ are the components of the EFG tensor, $eq = V_{zz}$ is the largest eigenvalue or principal component of the EFG, and $\eta = |V_{xx} - V_{yy}|/V_{zz}$ is the EFG asymmetry (here, the principal axes of EFG are chosen such that $|V_{zz}| \geq |V_{yy}| \geq |V_{xx}|$). Experimentally, the transitions can be observed at the frequency $\nu_z = \nu_Q \sqrt{1 + \eta^2/3}$.

The principal axes $\{x, y, z\}$ of the EFG tensor are defined by the local symmetry of the crystal structure. Consequently, the corresponding resonance frequency to any nuclear transition will have strong dependence on the direction of the applied field with respect to the crystallographic axes. For a site with axial symmetry ($\eta = 0$), there will be $2I - 1$ quadrupolar

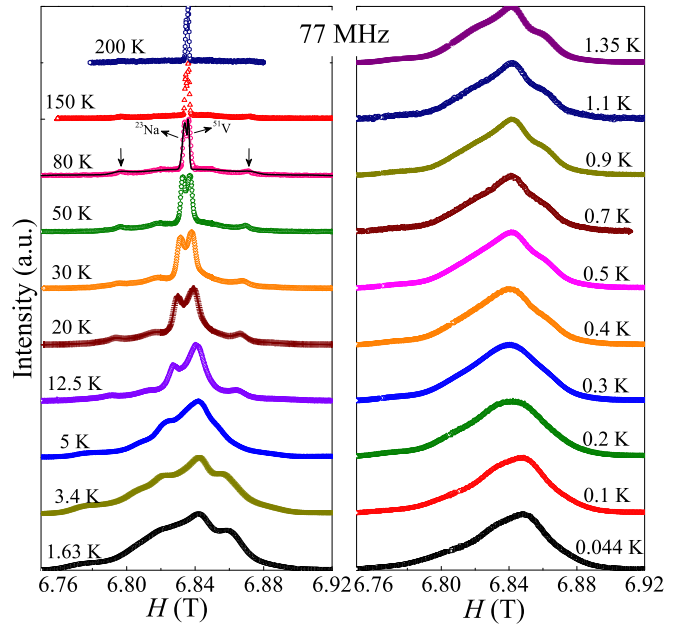


FIG. 7. Field-sweep NMR spectra of the polycrystalline $\text{BaNa}_2\text{Cu}(\text{VO}_4)_2$ sample, measured at 77 MHz as a function of temperature. The spectral lines corresponding to ^{23}Na and ^{51}V nuclei for $T = 80$ K are marked by arrows. The solid line is the simulated spectrum.

resonances at frequencies $n\nu_Q$, where $n = 1, \dots, 2I - 1$. When $\eta > 0$, the resonances are not equally spaced. The EFG is fully characterized by the parameters ν_z , η , and \hat{z} , where \hat{z} is the unit vector in the direction of the principal axis of the EFG with the largest eigenvalue. When the Zeeman term dominates over the quadrupole term, first-order perturbation theory is enough for describing the system. In such a scenario, for a quadrupole nucleus, equally spaced satellite peaks should appear on either side of the central peak separated by ν_Q [55].

The NMR spectra as a function of temperature measured by sweeping the magnetic field at 77 MHz are presented in Fig. 7. Since ^{23}Na and ^{51}V nuclei have nearly the same γ values, one expects their spectral lines to appear very close to each other. Further, ^{23}Na and ^{51}V are quadrupolar nuclei with nuclear spins $I = 3/2$ and $7/2$, respectively, and the transitions with $\Delta m = \pm 1$ are expected between the energy levels. Therefore, one would anticipate three NMR lines for ^{23}Na : one central line corresponding to $I_z = +1/2 \longleftrightarrow -1/2$ and two equally spaced satellite lines corresponding to $I_z = \pm 3/2 \longleftrightarrow \pm 1/2$ and seven NMR lines for ^{51}V : the central line being $I_z = +1/2 \longleftrightarrow -1/2$ and the satellite lines $I_z = \pm 1/2 \longleftrightarrow \pm 3/2 \longleftrightarrow \pm 5/2 \longleftrightarrow \pm 7/2$. Indeed, at high temperatures, we observed two sharp and prominent peaks at the resonance field position and two satellite peaks on either side of those. The central peak towards the low-field side is identified to be the signal coming from the ^{23}Na nuclei, while the one towards the high-field side appears to be the ^{51}V peak. In addition to the central peaks, two satellite peaks correspond to the ^{23}Na line. At high temperatures, the NMR spectra are found to be narrow and one can distinguish the ^{23}Na and ^{51}V signals. As the temperature is lowered, the line broadens asymmetrically and the central lines shift weakly

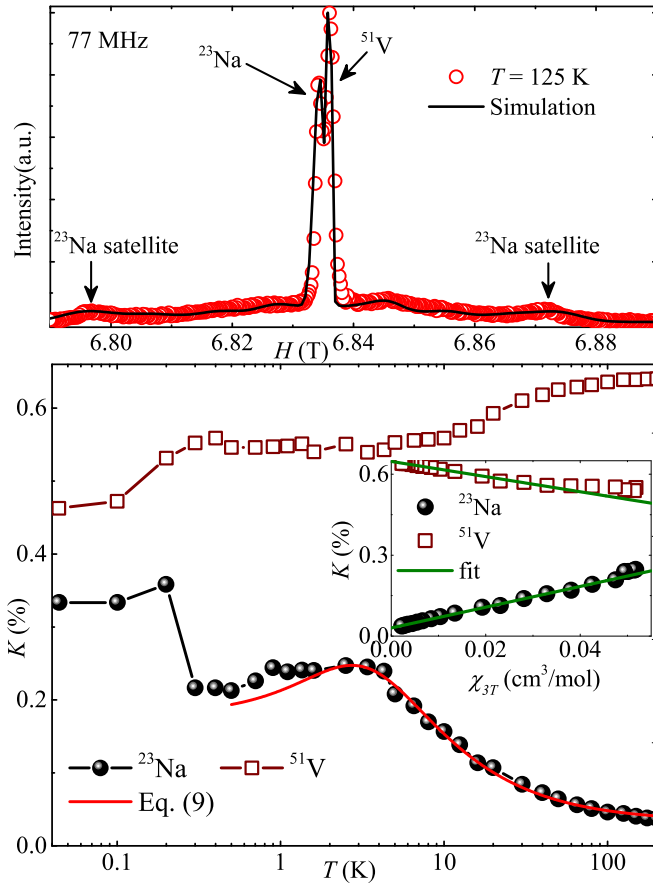


FIG. 8. Upper panel: NMR spectra at $T = 125$ K showing the ^{23}Na and ^{51}V central lines, with the downward arrows pointing to the ^{23}Na satellites. The solid line is the simulation of the spectra assuming the superposition of the ^{23}Na and ^{51}V signals. Lower panel: temperature-dependent NMR shift K as a function of temperature for ^{23}Na and ^{51}V , measured at 77 MHz. Solid line is the fit using Eq. (9). Inset: NMR shift vs χ measured at 3 T. Solid lines are the linear fits.

with temperature. No abrupt line broadening was noticed down to 44 mK, which may signal the absence of magnetic LRO [56]. The spectra were fitted assuming the superposition of ^{23}Na and ^{51}V signals. The spectral fit at $T = 125$ K is presented in the upper panel of Fig. 8, where ^{23}Na and ^{51}V lines and their satellites are marked by arrows. The obtained fitting parameters are $K \simeq 0.0345\%$ (isotropic shift), $\eta = 0$ (asymmetry parameter), and $\nu_Q \simeq 0.92$ MHz (NQR frequency) for ^{23}Na and $K \simeq 0.627\%$, $\eta = 0$, and $\nu_Q \simeq 0.234$ MHz for ^{51}V . The quadrupole frequency is found to be almost constant with temperature down to 1.5 K, which essentially excludes the possibility of any structural distortion in the studied compound.

The NMR shift $K(T)$ for both ^{23}Na and ^{51}V lines obtained from the spectral fits is plotted in the lower panel of Fig. 8. The temperature-dependent ^{23}Na shift [$^{23}K(T)$] is found to have a broad maximum at around 3 K, similar to the $\chi(T)$ data. As $K(T)$ is an intrinsic measure of the spin susceptibility χ_{spin} , one can write the linear relation

$$K(T) = K_0 + \frac{A_{\text{hf}}}{N_A \mu_B} \chi_{\text{spin}}, \quad (9)$$

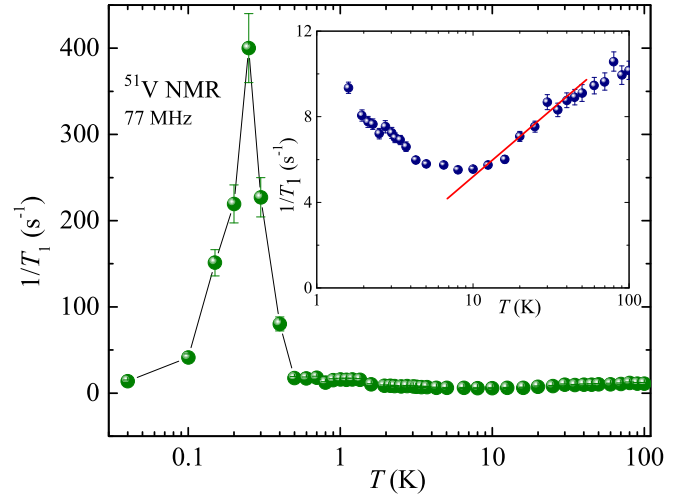


FIG. 9. $1/T_1$ as a function of temperature measured on the ^{51}V nuclei down to 0.044 K. Inset: $1/T_1$ above 2 K is shown in order to highlight the features around 10 K.

where K_0 is the temperature-independent chemical shift and the proportionality constant A_{hf} is the hyperfine coupling between the probed nuclei and the electron spins.

From Eq. (9), A_{hf} can be calculated by taking the slope of the linear K vs χ plot (inset of Fig. 8) with temperature as an implicit parameter. In the case of ^{23}Na , the data for $T \geq 5$ K were fitted well by a linear function, and the slope of the fit yields $^{23}A_{\text{hf}} \simeq 0.021$ T/ μ_B . Similarly, for ^{51}V the linearity is found over a large temperature range down to 10 K, and the linear fit returns $^{51}A_{\text{hf}} \simeq -0.016$ T/ μ_B . To estimate the exchange coupling, $^{23}K(T)$ above 2.5 K was fitted by Eq. (9) taking χ_{spin} for the 1D $S = 1/2$ Heisenberg chain [Eq. (3)]. The fit returns $J/k_B \simeq 4.22$ K and $^{23}A_{\text{hf}} \simeq 0.0194$ T/ μ_B . The value of g was fixed to $g = 2.17$ during the fitting procedure. This value of J/k_B is close to the one obtained from the $\chi(T)$ analysis, whereas $^{23}A_{\text{hf}}$ is also in good agreement with the value obtained from the K vs χ analysis. An anomaly at ~ 0.3 K in $^{23}K(T)$ could be due to a magnetic transition. To study the spin dynamics, spin-lattice relaxation rate ($1/T_1$) was measured by irradiating the central position of the ^{51}V spectra corresponding to the $1/2 \longleftrightarrow -1/2$ transition, choosing an appropriate pulse width. The recovery of the longitudinal magnetization was fitted by the following exponential function relevant for a quadrupole ($I = 7/2$) nuclei [57,58]

$$1 - \frac{M(t)}{M(\infty)} = 0.0119 \times e^{(-t/T_1)} + 0.068 \times e^{(-6t/T_1)} + 0.21 \times e^{(-15t/T_1)} + 0.71 \times e^{(-28t/T_1)}. \quad (10)$$

Here, $M(t)$ and $M(\infty)$ are the nuclear magnetizations at a time t and $t \rightarrow \infty$, respectively, after the saturation pulse. Temperature dependence of ^{51}V $1/T_1$ obtained from the above fit is shown in Fig. 9. Our measurements were carried out down to 0.04 K. At high temperatures, $1/T_1$ is almost temperature independent as expected in the paramagnetic regime [59]. At low temperatures, it exhibits a sharp peak at $T \simeq 0.25$ K due

to slowing down of the fluctuating moments and is a direct evidence of the onset of magnetic LRO. In order to highlight the behavior in the intermediate temperature range, $1/T_1$ above 2 K is magnified in the inset of Fig. 9. As the temperature is lowered, $1/T_1$ decreases linearly below about 25 K, remains almost temperature independent for $4 \text{ K} \leq T \leq 10 \text{ K}$, and then starts increasing for $T \leq 4 \text{ K}$. This increase below 4 K can be attributed to the growth of AFM correlations as the system approaches the magnetic LRO state.

Further, $1/T_1 T$ is directly proportional to the imaginary part of the dynamic susceptibility $\chi_M(\vec{q}, \omega_0)$ at the nuclear Larmor frequency ω_0 , which is q dependent [59]. In low-dimensional spin systems, temperature-dependent $1/T_1$ often reflects dominant contributions from different q values in different temperature regimes. For instance, for spin-1/2 Heisenberg AFM spin chains, it is theoretically predicted that with the dominant staggered contribution ($q = \pm\pi/a$) the spin-lattice relaxation rate behaves as $1/T_1 \sim T^0$, while the dominant contribution of the uniform component ($q = 0$) results in $1/T_1 \sim T$ [60,61]. The dominant contributions of $q = \pm\pi/a$ and $q = 0$ are typically observed in the low-temperature ($T < J$) and high-temperature ($T \sim J$) regimes, respectively [40,62]. Thus, our experimentally observed constant and linear behaviors of $1/T_1$ with temperature over $4 \text{ K} \leq T \leq 10 \text{ K}$ and $10 \text{ K} \leq T \leq 25 \text{ K}$, respectively (inset of Fig. 9), are compatible with the 1D physics.

In real spin-chain systems, the nonvanishing interchain couplings often lead to the onset of magnetic LRO at very low temperatures. The interchain coupling can be calculated using the expression proposed by Schulz [5]

$$\frac{|J_\perp|}{k_B} \simeq \frac{T_N}{1.28\sqrt{\ln(5.8J/(k_B T_N))}}, \quad (11)$$

where J_\perp is an effective interchain coupling. Taking $T_N \simeq 0.25 \text{ K}$ and $J/k_B \simeq 5.6 \text{ K}$, we arrive at the possible value of $J_\perp/k_B \simeq 0.1 \text{ K}$, which is indeed consistent with the value estimated from the band-structure calculations, as discussed in the following.

E. Microscopic magnetic model

LDA band structure of $\text{BaNa}_2\text{Cu}(\text{VO}_4)_2$ (Fig. 10) features Cu $3d$ states below the Fermi level and V $3d$ states above 2 eV, confirming the nonmagnetic state of vanadium. The overall energy spectrum is metallic, as typical for a transition-metal compound when correlation effects in the $3d$ shell were not taken into account. Nevertheless, this band structure gives an overview of possible exchange interactions, as the hopping parameters t_i are proportional to the LDA bandwidth, whereas $J_i^{\text{AFM}} = 4t_i^2/U_{\text{eff}}$. The Fermi level is crossed by two narrow bands formed by the half-filled $d_{x^2-y^2}$ orbitals of Cu^{2+} . The width of these bands is less than 0.2 eV, one of the smallest in cuprates, and indicates very weak exchange couplings in $\text{BaNa}_2\text{Cu}(\text{VO}_4)_2$.

DFT results for the exchange couplings are summarized in Table I. Only one sizable coupling, $J/k_B \simeq 6.8 \text{ K}$, is found. It corresponds to spin chains running along $[110]$ in one layer and along $[1\bar{1}0]$ in the adjacent layer, the direction being chosen by the position of the double VO_4 bridges that connect the CuO_4 plaquette units (Fig. 1). Such a coupling mechanism is

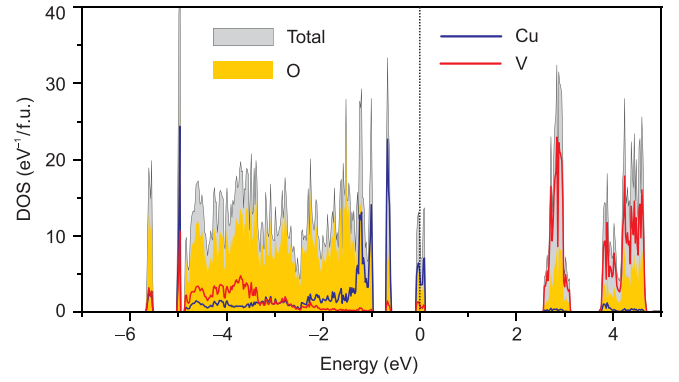


FIG. 10. LDA density of states for $\text{BaNa}_2\text{Cu}(\text{VO}_4)_2$. Note the very narrow Cu $d_{x^2-y^2}$ band around 0 eV (Fermi level) that indicates small electron hoppings and correspondingly weak exchange couplings.

fairly common among the Cu^{2+} compounds and can give rise to both FM and AFM superexchange depending on the orientation of the VO_4 tetrahedra relative to the CuO_4 planes [19]. Larger rotations of the tetrahedra favor FM couplings.

In $\text{BaNa}_2\text{Cu}(\text{VO}_4)_2$, we find $\varphi = 99.0^\circ$, which is similar to $\varphi^{(2)} = 102.2^\circ$ for the AFM coupling $J_a^{(2)}/k_B = 9.5 \text{ K}$ in $\text{BaAg}_2\text{Cu}(\text{VO}_4)_2$ and very different from $\varphi^{(1)} = 123.7^\circ$ for the FM coupling $J_a^{(1)}/k_B = -19 \text{ K}$ in the same compound [19]. Here, φ is the angle between the face of the VO_4 tetrahedron and the plane connecting the adjacent CuO_4 plaquettes, as shown in Fig. 1. Compared to $\text{BaAg}_2\text{Cu}(\text{VO}_4)_2$, the AFM coupling weakens from 9.5 K to $\sim 6 \text{ K}$, likely because of the longer Cu-Cu distance (5.507 Å vs. 5.448 Å) and the increased lateral displacement r of the CuO_4 plaquettes (0.895 Å vs 0.860 Å).

All couplings beyond the aforementioned spin chains appear to be very weak, below 0.2 K, and unfeasible for the DFT + U mapping analysis. Their relative strengths can be assessed from the hopping parameters that suggest the dominant interchain couplings J_{ab} in the ab plane (along $[1\bar{1}0]$ for the spin chains along $[110]$ and vice versa) and J_c along the c direction. The in-plane coupling J'_{ab} is negligible. The two stronger interchain couplings, J_{ab} and J_c , form a nonfrustrated 3D network. From $4t_i^2/U_{\text{eff}}$ with $U_{\text{eff}} = 5 \text{ eV}$ [41,63], one expects the coupling strength of 0.2 K or lower, in agreement with the DFT + U results. Altogether, our modeling results establish weak and nonfrustrated interchain couplings in $\text{BaNa}_2\text{Cu}(\text{VO}_4)_2$, with $J_\perp/J \simeq 0.02$. The average interchain

TABLE I. Exchange parameters of $\text{BaNa}_2\text{Cu}(\text{VO}_4)_2$ obtained from DFT calculations: Cu-Cu distances d (in Å), electron hoppings t_i (in meV), AFM contributions to the exchange $J_i^{\text{AFM}} = 4t_i^2/U_{\text{eff}}$ (in K), and total exchange couplings J_i (in K) from the DFT+ U mapping procedure.

	$d_{\text{Cu-Cu}}$	t_i	J_i^{AFM}/k_B	J_i/k_B
J	5.507	-40	14.9	6.8
J_{ab}	5.507	-5	0.2	< 0.2
J'_{ab}	5.686	-1	0.01	< 0.2
J_c	7.024	3	0.08	< 0.2

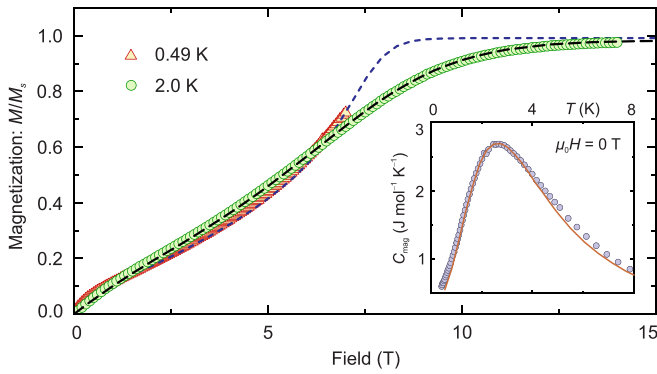


FIG. 11. Magnetization normalized to the saturation value (main figure) and magnetic specific heat (inset) of $\text{BaNa}_2\text{Cu}(\text{VO}_4)_2$. Predictions of the spin-chain model with $J/k_B = 5.5$ K and $g = 2.17$ are shown with lines. In magnetization curves, an additional 5% paramagnetic contribution described by the Brillouin function was included in order to reproduce the weak bend in low magnetic fields.

coupling of $J_\perp/k_B \simeq 0.1$ K leads to $k_B T_N/J \simeq 0.22$ [4] in good agreement with 0.25 K found experimentally. Therefore, we argue that long-range magnetic order in $\text{BaNa}_2\text{Cu}(\text{VO}_4)_2$ should be driven by weak interchain couplings, and the Néel temperature T_N/J is determined by the J_\perp/J ratio.

Above T_N , a purely one-dimensional description should hold. Indeed, we were able to fit magnetization curves down to 0.49 K using the spin-chain model with $J/k_B = 5.5$ K and $g = 2.17$ in excellent agreement with 5.6 K from the fit to the magnetic susceptibility and $g = 2.17(3)$ from the ESR experiment (Fig. 11). This confirms that the interchain couplings are very weak and play only a marginal role even at $T < J$. Magnetic specific heat is also well described by the spin-chain model showing small deviations below 1 K only. These deviations correspond to the upturn in C_{mag}/T upon approaching T_N (Fig. 6).

IV. CONCLUSIONS

We have shown that $\text{BaNa}_2\text{Cu}(\text{VO}_4)_2$ strongly deviates from all of its structural siblings in terms of the magnetic

behavior. The majority of these compounds are triangular magnets, while the only Cu^{2+} member studied to date, $\text{BaAg}_2\text{Cu}(\text{VO}_4)_2$, revealed a very unusual coexistence of different spin chains, one ferromagnetic and one antiferromagnetic [19,20]. Our present results for $\text{BaNa}_2\text{Cu}(\text{VO}_4)_2$ corroborate nontrivial magnetostructural correlations in Cu^{2+} vanadates, where the sign of a magnetic coupling strongly depends on the spatial orientation of the VO_4 tetrahedra relative to the spin chains and CuO_4 plaquette units.

The disparity of spin chains is absent in $\text{BaNa}_2\text{Cu}(\text{VO}_4)_2$, but now the chains adopt two different directions and form an unusual crossed pattern. Interestingly, this crossed pattern does not cause any magnetic frustration, because the Cu^{2+} ion of one chain sits exactly on top of the Cu^{2+} ion of the adjacent chain (Fig. 1). Then, each magnetic site has only one coupling to a spin chain of another direction, and not two couplings, as expected theoretically [22]. This fact highlights the importance of lateral displacements between the Cu^{2+} ions of the crossed chains to induce the frustration. Such displacements do not occur in $\text{BaNa}_2\text{Cu}(\text{VO}_4)_2$, but they may potentially appear in sister compounds, because even the substitution of Na^+ by Ag^+ causes significant structural changes, although the two ions are very similar in size. Alternatively, one may consider structure types with a weaker spatial separation between the crossed chains that, in turn, allows several nonequivalent interactions to form a frustrated topology even in the absence of lateral displacements [64–66].

ACKNOWLEDGMENTS

We would like to acknowledge SERB, India, for financial support bearing sanction Grant No. CRG/2019/000960. Work at the Ames Laboratory was supported by the U.S. Department of Energy, Office of Science, Basic Energy Sciences, Materials Sciences and Engineering Division. The Ames Laboratory is operated for the U.S. Department of Energy by Iowa State University under Contract No. DEAC02-07CH11358. A.A.T. was funded by the Federal Ministry for Education and Research through the Sofja Kovalevskaya Award of Alexander von Humboldt Foundation.

- [1] S. Sachdev, Quantum phase transitions, in *Handbook of Magnetism and Advanced Magnetic Materials* (John Wiley & Sons, Inc., 2007).
- [2] A. P. Ramirez, Strongly geometrically frustrated magnets, *Annu. Rev. Mater. Sci.* **24**, 453 (1994).
- [3] N. D. Mermin and H. Wagner, Absence of Ferromagnetism or Antiferromagnetism in One- or Two-Dimensional Isotropic Heisenberg Models, *Phys. Rev. Lett.* **17**, 1133 (1966).
- [4] C. Yasuda, S. Todo, K. Hukushima, F. Alet, M. Keller, M. Troyer, and H. Takayama, Néel Temperature of Quasi-Low-Dimensional Heisenberg Antiferromagnets, *Phys. Rev. Lett.* **94**, 217201 (2005).
- [5] H. J. Schulz, Dynamics of Coupled Quantum Spin Chains, *Phys. Rev. Lett.* **77**, 2790 (1996).
- [6] J. E. Greedan, Geometrically frustrated magnetic materials, *J. Mater. Chem.* **11**, 37 (2001).
- [7] K. M. Kojima, Y. Fudamoto, M. Larkin, G. M. Luke, J. Merrin, B. Nachumi, Y. J. Uemura, N. Motoyama, H. Eisaki, S. Uchida, K. Yamada, Y. Endoh, S. Hosoya, B. J. Sternlieb, and G. Shirane, Reduction of Ordered Moment and Néel Temperature of Quasi-One-Dimensional Antiferromagnets Sr_2CuO_3 and Ca_2CuO_3 , *Phys. Rev. Lett.* **78**, 1787 (1997).
- [8] T. Lancaster, S. J. Blundell, M. L. Brooks, P. J. Baker, F. L. Pratt, J. L. Manson, C. P. Landee, and C. Baines, Magnetic order in the quasi-one-dimensional spin- $\frac{1}{2}$ molecular chain compound copper pyrazine dinitrate, *Phys. Rev. B* **73**, 020410(R) (2006).

- [9] S. Furukawa, M. Sato, and S. Onoda, Chiral Order and Electromagnetic Dynamics in One-Dimensional Multiferroic Cuprates, *Phys. Rev. Lett.* **105**, 257205 (2010).
- [10] M. Hase, I. Terasaki, and K. Uchinokura, Observation of the Spin-Peierls Transition in Linear Cu^{2+} ($\text{Spin}-\frac{1}{2}$) Chains in an Inorganic Compound CuGeO_3 , *Phys. Rev. Lett.* **70**, 3651 (1993).
- [11] S.-L. Drechsler, O. Volkova, A. N. Vasiliev, N. Tristan, J. Richter, M. Schmitt, H. Rosner, J. Málek, R. Klingeler, A. A. Zvyagin, and B. Büchner, Frustrated Cuprate Route from Antiferromagnetic to Ferromagnetic $\text{Spin}-\frac{1}{2}$ Heisenberg Chains: $\text{Li}_2\text{ZrCuO}_4$ as a Missing Link near the Quantum Critical Point, *Phys. Rev. Lett.* **98**, 077202 (2007).
- [12] N. E. Amuneke, D. E. Gheorghe, B. Lorenz, and A. Möller, Synthesis, crystal structure, and physical properties of $\text{BaAg}_2\text{Cu}[\text{VO}_4]_2$: A new member of the $S = 1/2$ triangular lattice, *Inorg. Chem.* **50**, 2207 (2011).
- [13] A. Möller, N. E. Amuneke, P. Daniel, B. Lorenz, C. R. de la Cruz, M. Gooch, and P. C. W. Chu, $\text{A}\text{Ag}_2\text{M}[\text{VO}_4]_2$ ($\text{A} = \text{Ba}, \text{Sr}$; $\text{M} = \text{Co}, \text{Ni}$): A series of ferromagnetic insulators, *Phys. Rev. B* **85**, 214422 (2012).
- [14] G. Nakayama, S. Hara, H. Sato, Y. Narumi, and H. Nojiri, Synthesis and magnetic properties of a new series of triangular-lattice magnets, $\text{Na}_2\text{BaMV}_2\text{O}_8$ ($\text{M} = \text{Ni}, \text{Co}, \text{and Mn}$), *J. Phys.: Condens. Matter* **25**, 116003 (2013).
- [15] A. Reuß, V. Ksenofontov, J. Tapp, D. Wulferding, P. Lemmens, M. Panthöfer, and A. Möller, Screw-type motion and its impact on cooperativity in $\text{BaNa}_2\text{Fe}[\text{VO}_4]_2$, *Inorg. Chem.* **57**, 6300 (2018).
- [16] L. D. Sanjeewa, V. O. Garlea, M. A. McGuire, C. D. McMillen, and J. W. Kolis, Magnetic ground state crossover in a series of glaserite systems with triangular magnetic lattices, *Inorg. Chem.* **58**, 2813 (2019).
- [17] N. E. Amuneke, J. Tapp, C. R. de la Cruz, and A. Möller, Experimental realization of a unique class of compounds: XY-antiferromagnetic triangular lattices, $\text{KAg}_2\text{Fe}[\text{VO}_4]_2$ and $\text{RbAg}_2\text{Fe}[\text{VO}_4]_2$, with ferroelectric ground states, *Chem. Mater.* **26**, 5930 (2014).
- [18] S. Lee, R. Klauer, J. Menten, W. Lee, S. Yoon, H. Luetkens, P. Lemmens, A. Möller, and K.-Y. Choi, Unconventional spin excitations in the $S = \frac{3}{2}$ triangular antiferromagnet $\text{RbAg}_2\text{Cr}[\text{VO}_4]_2$, *Phys. Rev. B* **101**, 224420 (2020).
- [19] A. A. Tsirlin, A. Möller, B. Lorenz, Y. Skourski, and H. Rosner, Superposition of ferromagnetic and antiferromagnetic spin chains in the quantum magnet $\text{BaAg}_2\text{Cu}[\text{VO}_4]_2$, *Phys. Rev. B* **85**, 014401 (2012).
- [20] Y. Krupskaya, M. Schäpers, A.U.B. Wolter, H.-J. Grafe, E. Vavilova, A. Möller, B. Büchner, and V. Kataev, Magnetic resonance study of the spin-1/2 quantum magnet $\text{BaAg}_2\text{Cu}[\text{VO}_4]_2$, *Z. Phys. Chem.* **231**, 759 (2017).
- [21] M. von Postel and Hk. Müller-Buschbaum, $\text{Na}_2\text{BaCuV}_2\text{O}_8$: Ein neuer Strukturtyp der Alkali-Erdalkalimetall Kupfer-Oxovanadate, *Z. Anorg. Allg. Chem.* **618**, 107 (1992).
- [22] O. A. Starykh, R. R. P. Singh, and G. C. Levine, Spinons in a Crossed-Chains Model of a 2D Spin Liquid, *Phys. Rev. Lett.* **88**, 167203 (2002).
- [23] P. Sindzingre, J.-B. Fouet, and C. Lhuillier, One-dimensional behavior and sliding Luttinger liquid phase in a frustrated spin-1/2 crossed chain model: Contribution of exact diagonalizations, *Phys. Rev. B* **66**, 174424 (2002).
- [24] W. Brenig and M. Grzeschik, Valence-bond crystal phase of the crossed-chain quantum spin model, *Phys. Rev. B* **69**, 064420 (2004).
- [25] O. A. Starykh, A. Furusaki, and L. Balents, Anisotropic pyrochlores and the global phase diagram of the checkerboard antiferromagnet, *Phys. Rev. B* **72**, 094416 (2005).
- [26] R. F. Bishop, P. H. Y. Li, D. J. J. Farnell, J. Richter, and C. E. Campbell, Frustrated Heisenberg antiferromagnet on the checkerboard lattice: $J_1 - J_2$ model, *Phys. Rev. B* **85**, 205122 (2012).
- [27] J. Rodriguez-Carvajal, Recent advances in magnetic structure determination by neutron powder diffraction, *Physica B: Condensed Matter* **192**, 55 (1993).
- [28] K. Koepernik and H. Eschrig, Full-potential nonorthogonal local-orbital minimum-basis band-structure scheme, *Phys. Rev. B* **59**, 1743 (1999).
- [29] J. P. Perdew and Y. Wang, Accurate and simple analytic representation of the electron-gas correlation energy, *Phys. Rev. B* **45**, 13244 (1992).
- [30] H. J. Xiang, E. J. Kan, S.-H. Wei, M.-H. Whangbo, and X. G. Gong, Predicting the spin-lattice order of frustrated systems from first principles, *Phys. Rev. B* **84**, 224429 (2011).
- [31] O. Janson, A. A. Tsirlin, E. S. Osipova, P. S. Berdonosov, A. V. Olenov, V. A. Dolgikh, and H. Rosner, $\text{CaCu}_2(\text{SeO}_3)_2\text{Cl}_2$: Spin- $\frac{1}{2}$ Heisenberg chain compound with complex frustrated interchain couplings, *Phys. Rev. B* **83**, 144423 (2011).
- [32] S. Todo and K. Kato, Cluster Algorithms for General- S Quantum Spin Systems, *Phys. Rev. Lett.* **87**, 047203 (2001).
- [33] F. Alet, S. Wessel, and M. Troyer, Generalized directed loop method for quantum Monte Carlo simulations, *Phys. Rev. E* **71**, 036706 (2005).
- [34] A.F. Albuquerque, F. Alet, P. Corboz, P. Dayal, A. Feiguin, S. Fuchs, L. Gamper, E. Gull, S. Gürtler, A. Honecker, R. Igarashi, M. Körner, A. Kozhevnikov, A. Läuchli, S.R. Manmana, M. Matsumoto, I.P. McCulloch, F. Michel, R.M. Noack, G. Pawłowski, L. Pollet, T. Pruschke, U. Schollwöck, S. Todo, S. Trebst, M. Troyer, P. Werner, and S. Wessel, The ALPS project release 1.3: Open-source software for strongly correlated systems, *J. Magn. Magn. Mater.* **310**, 1187 (2007).
- [35] J. C. Bonner and M. E. Fisher, Linear magnetic chains with anisotropic coupling, *Phys. Rev.* **135**, A640 (1964).
- [36] S. Eggert, I. Affleck, and M. Takahashi, Susceptibility of the Spin $\frac{1}{2}$ Heisenberg Antiferromagnetic Chain, *Phys. Rev. Lett.* **73**, 332 (1994).
- [37] P. W. Selwood, *Magnetochemistry* (Read Books Ltd, New York, 1956).
- [38] Mendelsohn, Biggs, and Mann, Hartree-fock diamagnetic susceptibilities, *Phys. Rev. A* **2**, 1130 (1970).
- [39] N. Motoyama, H. Eisaki, and S. Uchida, Magnetic Susceptibility of Ideal Spin $\frac{1}{2}$ Heisenberg Antiferromagnetic Chain Systems, Sr_2CuO_3 and SrCuO_2 , *Phys. Rev. Lett.* **76**, 3212 (1996).
- [40] R. Nath, A. V. Mahajan, N. Büttgen, C. Kegler, A. Loidl, and J. Bobroff, Study of one-dimensional nature of $S = \frac{1}{2}$ $(\text{Sr,Ba})_2\text{Cu}(\text{PO}_4)_2$ and BaCuP_2O_7 via ^{31}P NMR, *Phys. Rev. B* **71**, 174436 (2005).
- [41] N. Ahmed, A. A. Tsirlin, and R. Nath, Multiple magnetic transitions in the spin- $\frac{1}{2}$ chain antiferromagnet $\text{SrCuTe}_2\text{O}_6$, *Phys. Rev. B* **91**, 214413 (2015).

- [42] M. Takigawa, P. C. Hammel, R. H. Heffner, Z. Fisk, J. L. Smith, and R. B. Schwarz, Anisotropic Cu Knight shift and magnetic susceptibility in the normal state of $\text{YBa}_2\text{Cu}_3\text{O}_7$, *Phys. Rev. B* **39**, 300 (1989).
- [43] A. Klümper, The spin-1/2 Heisenberg chain: Thermodynamics, quantum criticality and spin-Peierls exponents, *Eur. Phys. J. B* **5**, 677 (1998).
- [44] S. Lebernegg, A. A. Tsirlin, O. Janson, R. Nath, J. Sichelschmidt, Yu. Skourski, G. Amthauer, and H. Rosner, Magnetic model for $\text{A}_2\text{CuP}_2\text{O}_7$ ($\text{A} = \text{Na}, \text{Li}$): One-dimensional versus two-dimensional behavior, *Phys. Rev. B* **84**, 174436 (2011).
- [45] A. Abragam and B. Bleaney, *Electron Paramagnetic Resonance of Transition Ions* (Oxford University Press, Oxford, 2012).
- [46] B. I. Kochelaev, J. Sichelschmidt, B. Elschner, W. Lemor, and A. Loidl, Intrinsic EPR in $\text{La}_{2-x}\text{Sr}_x\text{CuO}_4$: Manifestation of Three-Spin Polarons, *Phys. Rev. Lett.* **79**, 4274 (1997).
- [47] R. Nath, K. M. Ranjith, J. Sichelschmidt, M. Baenitz, Y. Skourski, F. Alet, I. Rousochatzakis, and A. A. Tsirlin, Hindered magnetic order from mixed dimensionalities in CuP_2O_6 , *Phys. Rev. B* **89**, 014407 (2014).
- [48] V. A. Ivanshin, V. Yushankhai, J. Sichelschmidt, D. V. Zakharov, E. E. Kaul, and C. Geibel, ESR study of the anisotropic exchange in the quasi-one-dimensional antiferromagnet $\text{Sr}_2\text{V}_3\text{O}_9$, *Phys. Rev. B* **68**, 064404 (2003).
- [49] J. Sichelschmidt, M. Baenitz, C. Geibel, F. Steglich, A. Loidl, and H. H. Otto, Quasi-one-dimensional spin chains in CuSiO_3 : an EPR study, *Appl. Magn. Reson.* **23**, 75 (2002).
- [50] C. Kittel, *Introduction to Solid State Physics* (J. Wiley, Hoboken, NJ, c2005), p. 500317.
- [51] K. Caslin, R. K. Kremer, F. S. Razavi, A. Schulz, A. Muñoz, F. Pertlik, J. Liu, M.-H. Whangbo, and J. M. Law, Characterization of the spin- $\frac{1}{2}$ linear-chain ferromagnet CuAs_2O_4 , *Phys. Rev. B* **89**, 014412 (2014).
- [52] B. Bernu and G. Misguich, Specific heat and high-temperature series of lattice models: Interpolation scheme and examples on quantum spin systems in one and two dimensions, *Phys. Rev. B* **63**, 134409 (2001).
- [53] N. J. Curro, Nuclear magnetic resonance in the heavy fermion superconductors, *Rep. Prog. Phys.* **72**, 026502 (2009).
- [54] C. P. Slichter, *Principle of Nuclear Magnetic Resonance*, 3rd ed. (Springer, New York, 1992).
- [55] G. Lang, J. Bobroff, H. Alloul, P. Mendels, N. Blanchard, and G. Collin, Evidence of a single nonmagnetic Co^{3+} state in the Na_1CoO_2 cobaltate, *Phys. Rev. B* **72**, 094404 (2005).
- [56] K. M. Ranjith, R. Nath, M. Majumder, D. Kasinathan, M. Skoulatos, L. Keller, Y. Skourski, M. Baenitz, and A. A. Tsirlin, Commensurate and incommensurate magnetic order in spin-1 chains stacked on the triangular lattice in $\text{Li}_2\text{NiW}_2\text{O}_8$, *Phys. Rev. B* **94**, 014415 (2016).
- [57] M. I. Gordon and M. J. R. Hoch, Quadrupolar spin-lattice relaxation in solids, *J. Phys. C* **11**, 783 (1978).
- [58] W. W. Simmons, W. J. O'Sullivan, and W. A. Robinson, Nuclear spin-lattice relaxation in dilute paramagnetic sapphire, *Phys. Rev.* **127**, 1168 (1962).
- [59] T. Moriya, Nuclear magnetic relaxation in antiferromagnetics, *Prog. Theor. Exp. Phys.* **16**, 23 (1956).
- [60] A. Sandvik, NMR relaxation rates for the spin-1/2 Heisenberg chain, *Phys. Rev. B* **52**, R9831 (1995).
- [61] S. Sachdev, NMR relaxation in half-integer antiferromagnetic spin chains, *Phys. Rev. B* **50**, 13006 (1994).
- [62] R. Nath, D. Kasinathan, H. Rosner, M. Baenitz, and C. Geibel, Electronic and magnetic properties of $\text{K}_2\text{CuP}_2\text{O}_7$: A model $S = \frac{1}{2}$ Heisenberg chain system, *Phys. Rev. B* **77**, 134451 (2008).
- [63] S. Lebernegg, A. A. Tsirlin, O. Janson, and H. Rosner, Spin gap in malachite $\text{Cu}_2(\text{OH})_2\text{CO}_3$ and its evolution under pressure, *Phys. Rev. B* **88**, 224406 (2013).
- [64] A. A. Tsirlin, R. Nath, J. Sichelschmidt, Y. Skourski, C. Geibel, and H. Rosner, Frustrated couplings between alternating spin- $\frac{1}{2}$ chains in AgVOAsO_4 , *Phys. Rev. B* **83**, 144412 (2011).
- [65] P. K. Mukharjee, K. M. Ranjith, B. Koo, J. Sichelschmidt, M. Baenitz, Y. Skourski, Y. Inagaki, Y. Furukawa, A. A. Tsirlin, and R. Nath, Bose-Einstein condensation of triplons close to the quantum critical point in the quasi-one-dimensional spin- $\frac{1}{2}$ antiferromagnet NaVOPO_4 , *Phys. Rev. B* **100**, 144433 (2019).
- [66] F. Weickert, A. A. Aczel, M. B. Stone, V. O. Garlea, C. Dong, Y. Kohama, R. Movshovich, A. Demuer, N. Harrison, M. B. Gamza, A. Steppke, M. Brando, H. Rosner, and A. A. Tsirlin, Field-induced double dome and Bose-Einstein condensation in the crossing quantum spin chain system AgVOAsO_4 , *Phys. Rev. B* **100**, 104422 (2019).